A theoretical approximation of the shock stand-off distance for the flows around a circular cylinder

SINCLAIR, J and CUI, Xinjun <http://orcid.org/0000-0003-0581-3468>

A theoretical approximation of the shock standoff distance for supersonic flows around a circular cylinder

J. Sinclair and X. Cui

Citation: Physics of Fluids **29**, 026102 (2017); doi: 10.1063/1.4975983
View online: http://dx.doi.org/10.1063/1.4975983
View Table of Contents: http://aip.scitation.org/toc/phf/29/2
Published by the American Institute of Physics

A theoretical approximation of the shock standoff distance for supersonic flows around a circular cylinder

J. Sinclair and X. Cui[a)]
Aerospace Engineering, Department of Engineering and Mathematics, Sheffield Hallam University, Sheffield S1 1WB, United Kingdom

(Received 19 August 2016; accepted 25 January 2017; published online 22 February 2017)

Many previous studies have addressed the problem of theoretically approximating the shock standoff distance; however, limitations to these methods fail to produce excellent results across the entire range of Mach numbers. This paper proposes an alternative approach for approximating the shock standoff distance for supersonic flows around a circular cylinder. It follows the philosophy that the "modified Newtonian impact theory" can be used to calculate the size of the sonic zone bounded between the bow shock and the fore part of the body and that the variation of the said zone is related to the standoff distance as a function of the upstream Mach number. Consequently, a reduction rate parameter for the after-shock subsonic region and a reduction rate parameter for the shock standoff distance are introduced to formulate such a relation, yielding a new expression for the shock standoff distance given in Equation (32). It is directly determined by the upstream Mach number and the location of the sonic point at the body surface. The shock standoff distance found by this relation is compared with the numerical solutions obtained by solving the two-dimensional inviscid Euler equations, and with previous experimental results for Mach numbers from 1.35 to 6, and excellent and consistent agreement is achieved across this range of Mach numbers. *Published by AIP Publishing.* [http://dx.doi.org/10.1063/1.4975983]

I. INTRODUCTION

The study of the flows, in particular at supersonic and hypersonic speeds, around blunt bodies has been continuously attracting attention world-wide due to its theoretical difficulties and broad application background. It also remains as one of the most difficult areas to simulate numerically due to the complexities of the associated phenomena, e.g., shock waves, transition from subsonic to supersonic regions, viscous effect, and shock-boundary layer flow interaction. Among seven representative problems highlighted by Moretti[1] in his review of "computation of flows with shocks," the shock problems associated with the flow around circular obstacles were mentioned twice and were also among the most complicated. For example, even slight variation in the shock location may affect the drag coefficients, and the aircraft designer thus wants a stronger assurance of reliability. Therefore, the determination of the location and strength of the shocks remains as a critical task. One important parameter in this field of study is the shock standoff distance or detachment distance, i.e., the distance between the detached shock wave and the surface of the cylinder at the stagnation point, hereafter denoted as δ.

Many factors can be said to influence δ, e.g., Mach number, body profile, and gas properties. Due to the lack of a purely theoretical method to predict standoff distances, it is still necessary to produce even more accurate and widely applicable approximations for this parameter. Over the years, numerous studies have attacked the problem of formulating theoretical approximations for δ in gas dynamics. In an attempt to simplify this problem, different assumptions have been used, e.g., Moeckel's[2] hyperbolic shock shape, Hida's[3] rotational incompressible flow, and Lighthill's[4] assumption of a constant density behind the shock. A good review of these very early attempts is provided by Alperin[5] and Van Dyke.[6]

Experimental methods are still, to this day, the most accurate method of measuring δ; however, for high velocity flow these tests become costly, time consuming, and complex. Traditionally the use of wind tunnels or shock tubes coupled with Schlieren photography made it possible to experimentally determine δ. Alperin[5] carried out experimental investigation of the detached shock wave phenomena for the flow around a circular cylinder for Mach numbers from 1.35 to 2, but the shock standoff distance showed large disagreement with the theoretical results based on the stream function or potential theories. The experimental studies carried out by Kim[7] covered a broad range of Mach numbers from 1.35 to 6.0 but still showed no close agreement with some of the theoretical approximations, for example, of Hida's.[3] Similar experiments were also carried out by Moeckel[8] for studying the flow around axial symmetric bodies, by Heberle *et al.*[9] around cones and spheres, and by Bryson[10] around circular arc sections.

The flow with a detached shock wave becomes analytically difficult to solve since the location and the shape of a shock wave cannot be predicted in advance and the flow field in the shock region is highly vortical. Such vorticity effect was investigated by Hida[3] in his analytical approximation for the shock standoff distance for flows around a circular cylinder and a sphere, and he[11] later extended his work to hypersonic flows by assuming a perfect gas with a constant

[a)]Electronic mail: x.cui@shu.ac.uk. ORCID: 0000-0003-0581-3468.

specific heat ratio. Kaattari[12] achieved a good agreement with experiment for Mach numbers from 2 to 6 by adopting an inverted method where the body shape was used to determine the shock shape and location. Osborne and Crane[13] and Kaattari[14] showed that the modified Newtonian law can be applied to determine the location of the sonic points, providing a fairly well correlation with experimental studies for a variety of blunt bodies. Nagaraia[15] used the Newtonian centrifugal equation for pressure behind the shock to predict δ for blunt bodies in hypersonic flows.

Meanwhile, numerical analysis of the flow over circular cylinders has attracted wide attention too. For example, Beletoserkovski[16] and Hamaker[17] included non-isentropic conditions of the curved shock and vorticity for an inviscid perfect gas. Thoman and Szewczyk[18] produced time dependent results for viscous flow and Yang *et al.*[19] analysed shock wave diffraction using inviscid compressible Euler equations. Also, to improve the real world accuracy of the analysis of high velocity flows, non-equilibrium gases must be evaluated. Hornung[20] and Wen and Hornung[21] both introduced a reaction parameter in their theoretical approximations to account such effects. These studies provide better agreement with experimental data as the Mach number tends to infinity as these effects become more dominant. Further experimental and viscous numerical investigations include Trivandrum[22] and Mizukaki[23] who adopted a ballistic range and direction-indicating color Schlieren method for measuring the standoff distance for steel projectiles. With the application for Martian re-entry, Sharma *et al.*[24] conducted a CO_2 based experiment and numerical study. With the focus on re-entry vehicles, Zander *et al.*[25] coupled their hypervelocity numerical analysis with the experimental results obtained from expansion tunnel tests for spheres. Moreover, the power of modern computers makes it possible to apply direct numerical simulation to such complex problems, for example, Nagata *et al.*[26] carried out analysis for the flow properties around a sphere by numerically solving the three-dimensional compressible Navier-Stokes equations for the Mach number from 0.3 to 2.0 and Reynolds number from 50 to 300. This study highlights that the Reynolds number and thus the boundary layer are important factors influencing the size and shape of the shock, where the shock standoff distance increases as the Reynolds number decreases.

An interesting area that shares great commonalities and analogies in particular for the study of shock waves has emerged recently when the phenomena associated with the gravity-driven granular flow or shallow-water type flow are investigated. "Hydraulic bore" is an equivalent term of the shock wave for water flows, but "granular shock" becomes more acceptable for granular flows including natural hazardous and geophysical flows. A comprehensive study of the granular shock phenomena was carried out by Gray *et al.*,[27] where they generalized the hydraulic theory for snow avalanches to model granular flows over obstacles. In their study of the flow around a rearward facing pyramid, they captured the formation of the detached bow shock waves and showed good agreement between their numerical simulation and experiment. Another systematic study of the granular shocks was made by Gray and Cui[28] where they established an approach to the granular oblique shock theory that is analogous to gas dynamics. In particular they showed also the generation of the strong oblique shocks in their numerical and experimental study, confirming the prediction by the shock theory. Indeed many experimental and numerical studies have been carried out in this field in recent years, e.g., Refs. 29–35. A recent work by Cui and Gray[36] has been focused on the granular flow around a circular cylinder, where the bow shock wave was investigated for its development and formation and the relation of the standoff distance with the upstream Froude number.

Above all, these examples show that the study of the supersonic flow around circular cylinders and the determination of the standoff distance δ continue to be an important and even broader field of study. This paper aims to investigate an alternative theoretical approximation for δ for the flow around a circular cylinder. To provide a form of validation, quantitative data obtained by numerically solving the two-dimensional time-dependent Euler equations shall be utilized, addressed in Sec. II.

II. A DESCRIPTION OF THE COMPUTATION TECHNIQUES

Until Abbett and Moretti's breakthrough,[37] solving the blunt body problem numerically was not possible, due to elliptic and hyperbolic equations which were needed for subsonic and supersonic flows separately. Since then various computational techniques for evaluating shock inclusive flow fields have been developed. Among these, the TVD (total variation diminishing) schemes based on Harten[38] and the NOC (non-oscillatory central) schemes based on Nessyahu and Tadmor[39] are two popular methods in modern shock capturing techniques. In our simulation, an approximate Riemann solver developed by Roe[40] shall be used. It is a standard upwind flux difference splitting technique, based on the shock capturing numerical method by Godunov.[41]

A. Governing equations

For this numerical study, the governing conversational time-dependent inviscid Euler equations are given as two-dimensional, in the following Cartesian (x,y) form:

$$\frac{\partial u}{\partial t} + \frac{\partial(\rho u)}{\partial x} + \frac{\partial(\rho v)}{\partial y} = 0, \tag{1}$$

$$\frac{\partial(\rho u)}{\partial t} + \frac{\partial(\rho u^2)}{\partial x} + \frac{\partial(\rho uv)}{\partial y} = -\frac{\partial p}{\partial x}, \tag{2}$$

$$\frac{\partial(\rho v)}{\partial t} + \frac{\partial(\rho uv)}{\partial x} + \frac{\partial(\rho v^2)}{\partial y} = -\frac{\partial p}{\partial y}, \tag{3}$$

$$\frac{\partial \rho e_t}{\partial t} + \frac{\partial(\rho e_t + p)u}{\partial x} + \frac{\partial(\rho e_t + p)v}{\partial y} = 0, \tag{4}$$

where u and v are the velocity components, respectively, ρ is the density, and p the pressure. The heat transfer is neglected here, and the total specific energy is

$$e_t = \frac{1}{\gamma - 1}\frac{p}{\rho} + \frac{1}{2}(u^2 + v^2). \tag{5}$$

Defining these in the differential vector form gives

$$\frac{\partial U}{\partial t} + \frac{\partial F}{\partial x} + \frac{\partial G}{\partial y} = 0, \tag{6}$$

where

$$\mathrm{U} = \begin{bmatrix} \rho \\ \rho u \\ \rho v \\ \rho e_t \end{bmatrix}, \mathrm{F} = \begin{bmatrix} \rho u \\ \rho u^2 + p \\ \rho uv \\ \rho uh \end{bmatrix}, \mathrm{G} = \begin{bmatrix} \rho v \\ \rho vu \\ \rho v^2 + p \\ \rho vh \end{bmatrix}, \tag{7}$$

and the specific enthalpy is given by

$$h = e_t + \frac{p}{\rho}. \tag{8}$$

The above governing equations are then numerically solved using a finite volume method under appropriate boundary conditions. For simplicity we here leave such numerical details in Appendix A, and we shall now address the use of the mesh adaption technique, which is shown to be highly effective for resolving shock waves with high accuracy.

B. Mesh adaption

The formation of shock waves in the flow field leads to certain accuracy difficulties for numerical schemes due to the extremely or infinitely large gradients across the shock. A very effective tool to further improve the numerical accuracy in these regions is to adopt a solution-adaptive grid refinement, for example, a solution-adaptive gradient refinement in our case.

The grid is adapted by multiplying the Euclidean norm of the gradient ∇f for the selected variable f by the length scale (e.g., the work of Daunenhofer and Baron[42]). In this case, it corresponds to the density and the square of the cell volume, with the error indicator e_{i1} being computed by

$$|e_{i1}| = (A_{cell})^{\frac{r}{2}} |\nabla f|, \tag{9}$$

where A_{cell} denotes a cell area weighted by a gradient volume factor r. In the computation, after the solution was obtained

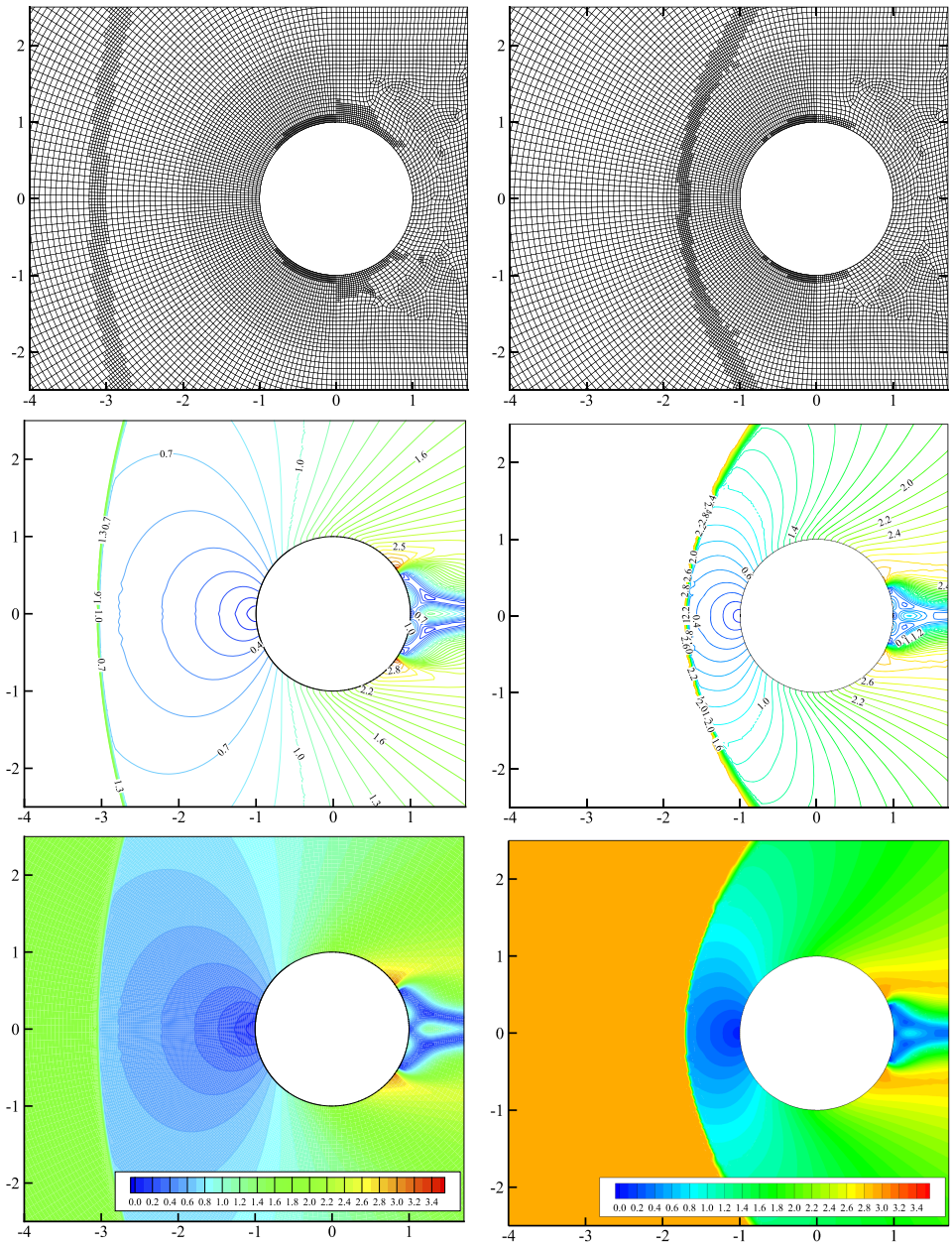

FIG. 1. Examples of the mesh adaptation technique applied for varying Mach numbers. The left hand side mesh is for $M_\infty = 1.7$, and the right hand mesh for $M_\infty = 3$, where the adapted region moves accordingly with the shock region.

using a normal mesh, a gradient adaption with a refined threshold of 10% of the maximum density value was applied. This continued until no additional iterations were required to converge the solution between each relative grid. Fig. 1 shows an example of such a method for two free stream Mach numbers of 1.7 and 3. Clearly, the adapted regions vary accordingly with the change of the location of the shock waves. It is also noticed that some refinements were performed in regions close to the body surface, in particular to the top and bottom areas of the cylinder, indicating a rapid density change in these regions too. Further results are given in Appendix B, see Figs. 12 and 13, and all these clearly indicate that excellent shock resolution was achieved using this approach.

The Mach number contours in Fig. 1 (and the velocity contours in Fig. 10 of Appendix B) also show the formation of recirculation zones after the flow detaches at the rear of the circular cylinder, and it is observed that these zones become stable for all Mach numbers in the tested range, i.e., $M_\infty = 1.35$ to 6.0, after the solutions converge to a steady state. However, a study by Salas[43] states that these zones fail to reach a stable state even for a low supersonic condition. On the other hand, studies for the transonic flow (e.g., the works of Moretti,[1] Pandolfi and Larocca,[44] Botta,[45] and Hafez and Wahba[46]) suggest unsteady periodic patterns for such recirculation zones. Further study to whether the absence of such periodic oscillations at the supersonic region is a result of the supersonic nature of the flow or due to any numerical simplification could reveal some interesting insight.

III. THEORETICAL APPROACH

A. The modified Newtonian law

For the flow around blunt bodies, Lees[47] proposed a modification to the Newtonian impact theory in a form

$$\frac{C_p}{C_{p,max}} = \sin^2\theta, \tag{10}$$

where θ is the angle of the body surface tangent to the free stream flow direction, as shown in Fig. 2. The pressure

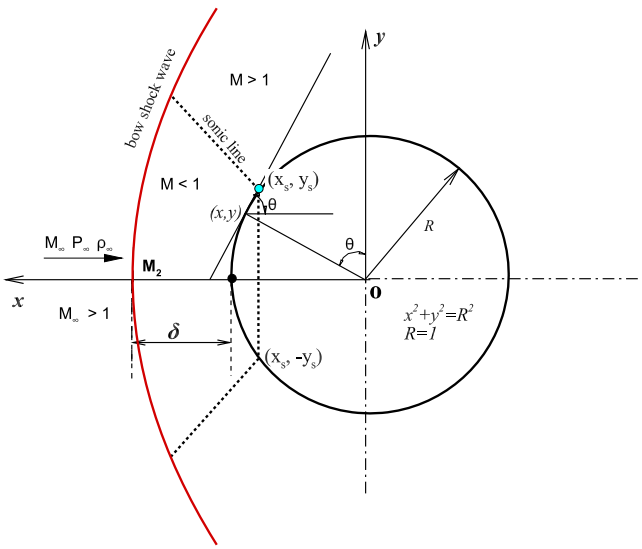

FIG. 2. A schematic showing the geometry of the flow field.

coefficient C_p is

$$C_p = \frac{2}{\gamma M_\infty^2}\left(\frac{p}{p_\infty} - 1\right), \tag{11}$$

where p is the surface static pressure on the circular cylinder. Using subscript "2" to denote the immediate after-shock conditions on the stagnation stream line, i.e., the central line in Fig. 2, the standard normal shock relation then gives

$$\frac{p_2}{p_\infty} = 1 + \frac{2\gamma}{\gamma+1}\left(M_\infty^2 - 1\right). \tag{12}$$

It is understood that for supersonic flows typical changes associated with thermodynamic properties occur across the shock wave, such as the increase in entropy and the drop of the stagnation (or total) pressure, but the stagnation (or total) temperature is still unchanged due to the conservation of energy. Hypersonic flows could be even more complicated since phenomena, for example, entropy layer, shock-boundary layer interaction, and non-equilibrium effect of gases become more dominant. Our discussion here shall focus on supersonic flows, with the assumption that the flow after the shock waves is regarded isentropic when no further shock waves occur. This feature is also further confirmed in our CFD (computational fluid dynamics) computations, for example, as shown in Fig. 11 in Appendix B. It means that the stagnation pressure after the shock, p_{02}, is constant too for the flow field between the shock and the fore part of the body, which can be given by

$$\frac{p_{02}}{p_2} = \left(1 + \frac{\gamma-1}{2}M_2^2\right)^{\frac{\gamma}{(\gamma-1)}}, \tag{13}$$

where the after-normal-shock Mach number

$$M_2 = \sqrt{\frac{2 + (\gamma-1)M_\infty^2}{2\gamma M_\infty^2 - \gamma + 1}}. \tag{14}$$

Considering a surface point on the cylinder with a Mach number M with respect to the static pressure p, we can have a similar relation to (13),

$$\frac{p_{02}}{p} = \left(1 + \frac{\gamma-1}{2}M^2\right)^{\frac{\gamma}{(\gamma-1)}}. \tag{15}$$

Therefore, the static pressure coefficient C_p of (11) can be obtained by combining Eqs. (12), (13), and (15) such that

$$\frac{p}{p_\infty} = \frac{p}{p_{02}} \cdot \frac{p_{02}}{p_2} \cdot \frac{p_2}{p_\infty}. \tag{16}$$

Consequently, the stagnation pressure coefficient $C_{p,max}$ is achieved when M = 0, in a form

$$C_{p,max} = \frac{2}{\gamma M_\infty^2}\left\{\left[\frac{(\gamma+1)^2 M_\infty^2}{4\gamma M_\infty^2 - 2(\gamma-1)}\right]^{\frac{\gamma}{\gamma-1}} \times \left[\frac{1-\gamma+2\gamma M_\infty^2}{\gamma+1}\right] - 1\right\}. \tag{17}$$

On the other hand, at the sonic point where $M_s = 1$, the corresponding surface pressure coefficient C_{ps} can be obtained in a similar manner. Substituting $M_s = 1$ first into Equation (15) gives

$$\frac{p_s}{p_{02}} = \left(\frac{\gamma+1}{2}\right)^{-\frac{\gamma}{\gamma-1}}, \tag{18}$$

where p_s is the static pressure at the surface sonic point of the cylinder. Then further substituting (12), (13), and (18) into (11) yields

$$C_{ps} = \frac{2}{\gamma M_\infty^2}\left\{\left(\frac{\gamma+1}{2}\right)^{-\frac{\gamma}{\gamma-1}}\left[\frac{(\gamma+1)^2 M_\infty^2}{4\gamma M_\infty^2 - 2(\gamma-1)}\right]^{\frac{\gamma}{\gamma-1}} \times\left[\frac{1-\gamma+2\gamma M_\infty^2}{\gamma+1}\right]-1\right\}. \tag{19}$$

We can now calculate $C_{p,max}$ and C_{ps} according to (17) and (19), respectively. With the specific heat ratio $\gamma = 1.4$, Fig. 3 shows the variation of C_{ps} and $C_{p,max}$ for the free stream Mach number from 1 to 10, where the coefficients increase rapidly only for lower Mach numbers, say, up to around 3 to 4. In particular, when $M_\infty = 1$, $C_{ps} = 0$, and $C_{p,max} = 1.2756$. When $M_\infty \to \infty$, the limiting values are $C_{ps} = 0.9717$ and $C_{p,max} = 1.8394$, respectively.

B. The sonic point at the cylinder surface

For the simplicity of discussion, let the radius of the circular cylinder $R = x^2 + y^2 = 1$, which can be achieved through the non-dimensionalization of the length scales. Denote the coordinates of the sonic point as (x_s,y_s), as shown in Fig. 4; the inclination angle of the surface sonic point, θ_s, has relations such that $\sin\theta_s = x_s$, $\cos\theta_s = y_s$. Further let $\theta_s + \beta_s = \frac{\pi}{2}$, the arc length from the sonic point to the stagnation point (or the leading edge point) on the cylinder is $L_s = R\beta_s = \beta_s$. Based on (10), we can establish a relation for β_s in such a form

$$\beta_s = \frac{\pi}{2} - \sin^{-1}\sqrt{\frac{C_{ps}}{C_{p,max}}}. \tag{20}$$

Note also that the angle β_s must be given in radians when used to calculate L_s.

Clearly, with the increase of the free stream Mach number, the subsonic region that is bounded by the sonic lines decreases too. For this reason, we denote β_s as the surface sonic angle, and its variation with M_∞ is shown in Fig. 5 with $\gamma = 1.4$. Also shown in the figure are the variation of the after-normal-shock

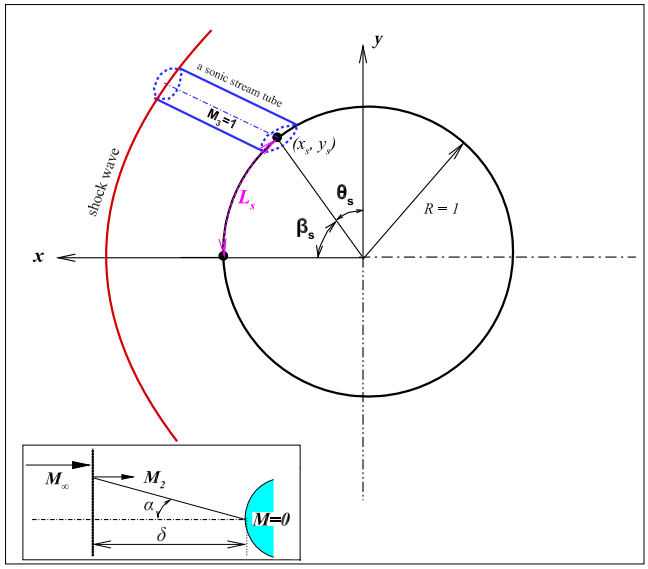

FIG. 4. Schematic showing the sonic point location, (x_s,y_s), on the cylinder surface. A "sonic stream tube" is also illustrated in the diagram, where the corresponding Mach number $M_3 = 1$ in the tube. The bottom-left inset shows a linear Mach number profile between the shock and the body on the central stagnation stream line, where δ is the shock standoff distance, and α represents an angle between the Mach number line and central stagnation stream line.

Mach number M_2 (in dashed-dotted line) and the variation of the density ratio across the normal shock ρ_∞/ρ_2 (in dashed line) based on

$$\frac{\rho_\infty}{\rho_2} = \frac{2+(\gamma-1)M_\infty^2}{(\gamma+1)M_\infty^2}. \tag{21}$$

In the figure, the labels for M_2 and ρ_∞/ρ_2 are marked on the vertical axis on the right-hand-side. In particular, when $M_\infty = 1$, $\beta_s = 90°$ thus $\theta_s = 0°$, $M_2 = 1$, and $\rho_\infty/\rho_2 = 1$; when $M_\infty \to \infty$, $\beta_s = 43.3787°$, $\theta_s = 46.6213°$, $M_2 = 0.3780$, and $\rho_\infty/\rho_2 = \frac{1}{6}$.

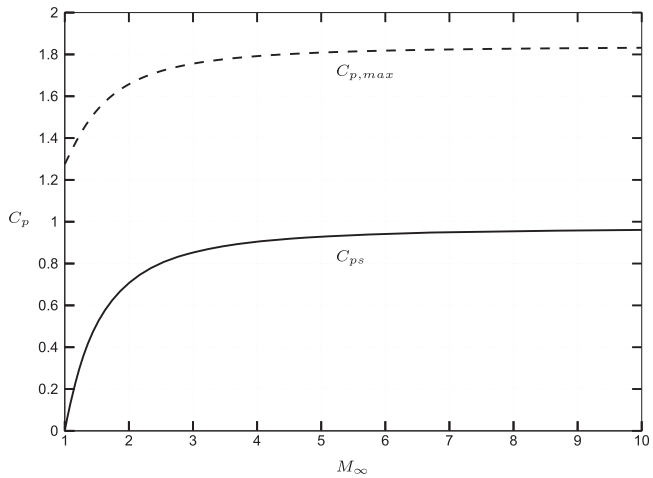

FIG. 3. Variation of the surface sonic pressure coefficient C_{ps} and stagnation pressure coefficient $C_{p,max}$ with the free stream Mach number M_∞, where $\gamma = 1.4$.

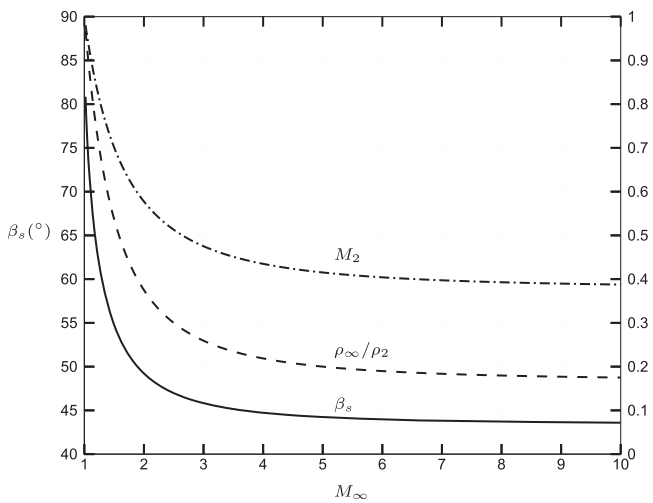

FIG. 5. Variation of the surface sonic angle β_s (in degrees here), M_2 and ρ_∞/ρ_2 with the free stream Mach number M_∞, where $\gamma = 1.4$.

C. A theoretical approximation to the shock standoff distance

1. Reduction rate parameter for the after-shock subsonic region, b_{ys}

In his experimental measurement of the shock standoff distance for hypersonic flows around spheres, Lobb[48] shows that the ratio of the standoff distance δ to the sphere diameter D correlates with the ratio of the free stream density ρ_∞ to the after-normal-shock density ρ_2 on the central stagnation stream line in such a relation

$$\frac{\delta}{D} = 0.41\frac{\rho_\infty}{\rho_2}. \tag{22}$$

This is followed by further experimental and theoretical studies on equilibrium and non-equilibrium hypersonic flows over spheres and circular cylinders, e.g., the works of Hornung,[20] Wen and Hornung,[21] and Olivier.[49] Because the standoff distance is related to the average density between the shock wave and the body on the stagnation stream line (or central line), a linear density profile is assumed if the density on the body is smaller than the equilibrium density.[21] Indeed, such a linear density profile does show a good agreement even with our simulation results, as shown in Fig. 13 (see Appendix B). However, while (22) may show a good agreement for the shock standoff distance for hypersonic flows, it fails to provide a consistent agreement for lower supersonic cases in particular when M_∞ is close to 1 since theoretically, δ/D becomes infinitely large but (22) only limits it to 0.41 as $\rho_\infty/\rho_2 \to 1$.

Instead of assuming a linear density profile, we now adopt a different approach. Consider a "sonic stream tube" in a flow field between the after-shock region and the body, denoted by subscript "3", as shown in Fig. 4. The conservation of continuity requires that the mass flow rate in this region, $\dot{m}_3 = \rho_3 A_3 v_3$, is constant, where ρ_3, A_3, and v_3 are the density, cross-sectional area, and velocity at a location of the stream tube, respectively. Assuming an isentropic condition for perfect gases, we can further re-write $\dot{m}_3$ into

$$\begin{aligned}\dot{m}_3 &= \rho_3 A_3 v_3 \\ &= \frac{p_{03} A_3 M_3 \sqrt{\gamma}}{\sqrt{R_g T_{03}}}\left(1 + \frac{\gamma-1}{2}M_3^2\right)^{-\frac{\gamma+1}{2(\gamma-1)}} = \text{constant},\end{aligned} \tag{23}$$

where R_g represents the gas constant. For the stagnation quantities, the isentropic assumption gives that $p_{03} = p_{02}$, $T_{03} = T_{02}$, where p_{02} and T_{02} can be obtained through the after-normal-shock relation, for example, Equation (13). Therefore, we can specify the sonic stream tube with the following conditions: p_{03} = constant, T_{03} = constant, and $M_3 = 1$. Further with γ and R_g being fixed, we can conclude from (23) that any cross-sectional area of the sonic stream tube, A_3, remains constant irrespectively, at least in an implicit way, of the free stream Mach number M_∞.

As previously discussed in Sec. III B, the after-shock subsonic region bounded by the sonic lines reduces with the increasing M_∞, from infinitely large when $M_\infty \to 1$ to an approximately fixed value when $M_\infty \to \infty$, we thus introduce a subsonic region parameter b in the following form:

$$b = \frac{A_3}{\theta_s} = \frac{A_3}{\cos^{-1} y_s}. \tag{24}$$

Since the cross-sectional area of the sonic stream tube A_3 only has a finite value, b varies inversely with the angle θ_s, from infinitely large as $M_\infty \to 1$ to a limiting value as $M_\infty \to \infty$ too, indicating a similar trend to the subsonic region. We may further assume that b is a primary function of y_s, while the variation of A_3 only has a secondary effect. Therefore, the reduction rate of this subsonic region with M_∞ can be represented by the following parameter:

$$b_{ys} = \frac{db}{dy_s} = \frac{A_3}{\sqrt{1-y_s^2}\left(\cos^{-1} y_s\right)^2}. \tag{25}$$

With the geometrical relation for the unit circular cylinder shown in Fig. 4, we have $x_s = \sqrt{1-y_s^2} = \cos\beta_s$ and $y_s = \cos\theta_s$, so (25) can be re-written as

$$b_{ys} = \frac{A_3}{\theta_s^2 \cos\beta_s}. \tag{26}$$

Fig. 6 shows a variation of the subsonic region parameter b and its reduction rate parameter b_{ys} with M_∞, where A_3 is chosen 1. The variation of b_{ys} is promising since it tends to maintain both the dramatic drop for low M_∞ and the asymptotical approach for high M_∞. On the other hand, the use of the cross-sectional area parameter A_3 is also interesting since it could further reshape the b-curve. Since A_3 is related with the sonic region, one direct and sensible choice is to let $A_3 = L_s^2$, where L_s is the arc length from the sonic point of the upper surface to the stagnation point of the body, as shown in Fig. 4. With the unit circular cylinder geometry, we have $L_s = \beta_s$, thus $A_3 = \beta_s^2$. Other alternative representations for A_3 have also been attempted in the preliminary study, but this L_s^2 choice is shown to offer a better result. Therefore, we can define a reduction rate parameter for the after-shock subsonic region in such a form

$$b_{ys} = \frac{\beta_s^2}{\theta_s^2 \cos\beta_s}. \tag{27}$$

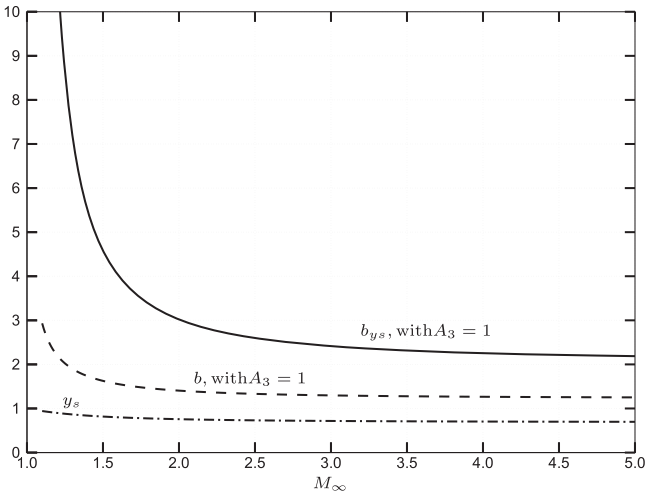

FIG. 6. Variation of b, b_{ys}, and y_s with the free stream Mach number M_∞.

2. Reduction rate parameter for the shock standoff distance, δ_{M_2}

As mentioned in Sec. III C 1, linear density profiles between the shock and the body have been used in many previous studies, but we here assume a linear Mach number profile on the stagnation stream line instead. As shown in the inset of Fig. 4, let δ be the standoff distance between the shock and the body and α be the angle formed between the Mach number line and the central stagnation stream line, then we have

$$\delta = \frac{M_2}{\tan\alpha}. \tag{28}$$

The dependence of δ on M_2 and $\tan\alpha$ can be rather complicated. Since M_2 only varies as a finite value regardless of the variation of M_∞, $\tan\alpha$ may thus be required to change from 0 (as $M_\infty \to 1$) to ∞ (as $M_\infty \to \infty$) so as to accommodate the corresponding variation for δ. With respect to the above, we can define the range for α from 0 to $\pi/2$. To make it comparable with b_{ys}, we introduce a reduction rate parameter for the shock standoff distance in such a manner

$$\delta_{M_2} = \frac{\partial\delta}{\partial M_2} = \frac{\partial}{\partial M_2}\left(\frac{M_2}{\tan\alpha}\right) = \cot\alpha. \tag{29}$$

Obviously, δ_{M_2} represents a rate of change of the shock standoff distance with respect to the after-normal-shock Mach number M_2. With the linear Mach number profiles' assumption, it is simply equal to $\cot\alpha$. However, this simple relation shows an interesting and reasonable representation for the variation of δ_{M_2} with M_∞: when M_∞ is low (i.e., close to 1), α is also small (close to 0), so $\cot\alpha$, hence δ_{M_2}, changes dramatically; when M_∞ is relatively high, say, above 5, α can be "tuned" close to $\pi/2$, hence the value of $\cot\alpha$ is close to zero already, which means δ_{M_2} is small and the standoff distance δ is then close to a small and almost constant value. Therefore, such a variation behavior for δ_{M_2} is at least consistent with, or might even be a good approximation for the variation of δ if $\cot\alpha$ could be properly represented.

3. A proposed method: $b_{ys} = \delta_{M_2}$

After the discussions in Secs. III C 1 and III C 2, finding a good representation for δ_{M_2}, the reduction rate parameter for shock standoff distance, becomes the most important task. In Sec. III C 2, a term "tuned" was deliberately used when discussing the change for $\cot\alpha$. It makes us to almost naturally link δ_{M_2} with b_{ys}, another parameter representing the reduction rate for the subsonic region between the shock and the body, possibly based on these two reasons. First, they both possess a similar variational behavior with M_∞, that is, changing from infinitely large to a very small value at a rapid rate. Second, b_{ys} itself carries abundant information about how a detached shock, and consequently the subsonic region it has induced, would vary with the free stream conditions, e.g., M_∞, and with the body surface conditions, e.g., y_s. We therefore use b_{ys} to "tune" δ_{M_2} in its simplest form

$$\delta_{M_2} = \cot\alpha = b_{ys} = \frac{\beta_s^2}{\theta_s^2\cos\beta_s}. \tag{30}$$

With (28), the shock standoff distance is then formulated as

$$\delta = \frac{M_2\beta_s^2}{\theta_s^2\cos\beta_s}. \tag{31}$$

IV. DISCUSSION OF THE RESULT

A. Approximation of the shock standoff distance

Combining (31) with (14), the shock standoff distance can be re-written as

$$\delta = \frac{\beta_s^2}{\theta_s^2\cos\beta_s}\cdot\sqrt{\frac{2+(\gamma-1)M_\infty^2}{2\gamma M_\infty^2-\gamma+1}}. \tag{32}$$

Note that δ here is already non-dimensionalized by the radius of the circular cylinder since $R = 1$, and it is obtained under the assumption of a linear Mach number profile between the shock and the body on the central stagnation stream line. In Fig. 7, the normalized shock standoff distance, δ/D, obtained according to (32) is shown by the solid line. Surprisingly, an excellent agreement of it is shown with the experimental results by Alperin[5] that are drawn as filled diamond symbols, with the experimental results by Kim[7] as filled circle symbols, and also with our computational results as hollow square symbols, for a Mach number range from 1.35 to 6. This excellent agreement for the lower supersonic range, say, for Mach numbers up to 3, might be of particular interest since most of the available theoretical methods have so far failed to show a better agreement. Also shown in the same figure are some results that are obtained using different methods, as explained below.

If adopting a linear density profile instead, without repeating the details of similar derivations, we may establish an alternative relation for the shock standoff distance in such a form

$$\delta = \frac{\beta_s^2}{\theta_s^2\cos\beta_s}\cdot\frac{\rho_\infty}{\rho_2} = \frac{\beta_s^2}{\theta_s^2\cos\beta_s}\cdot\frac{2+(\gamma-1)M_\infty^2}{(\gamma+1)M_\infty^2}. \tag{33}$$

In Fig. 7, the result for δ/D obtained from (33) is shown in dotted lines, where a significant difference is seen with the above

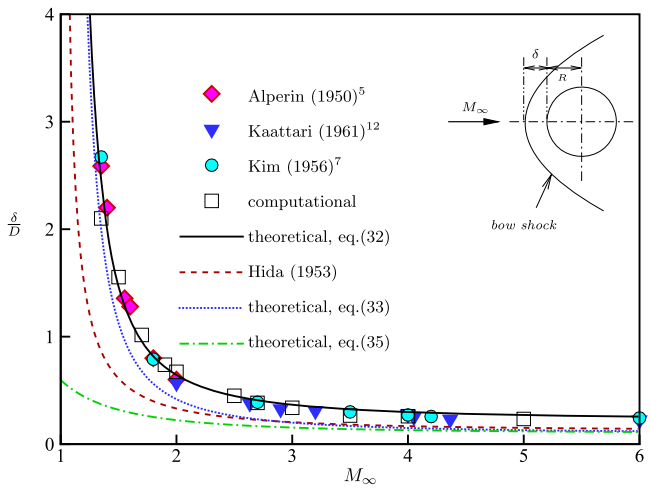

FIG. 7. The non-dimensional shock standoff distance $\frac{\delta}{2R}$ as a function of the free stream Mach number M_∞ obtained by different methods, where $\gamma = 1.4$.

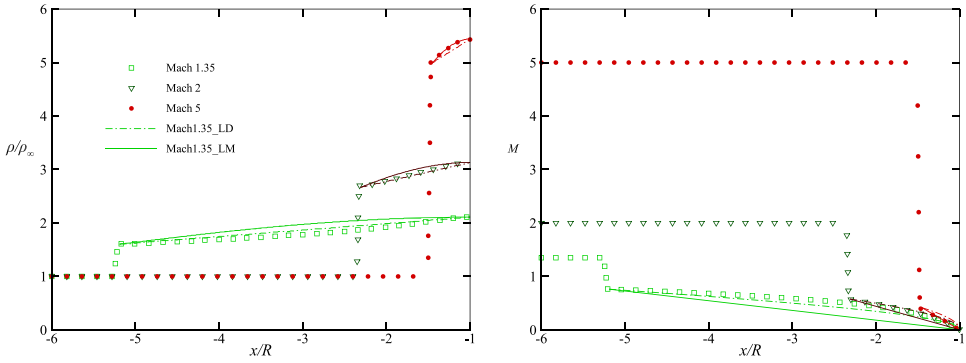

FIG. 8. Variation of ρ/ρ_∞, M with x/R on the central stagnation stream line for the free stream $M_\infty = 1.35, 2, 5$. The scattered symbols represent computational results, the solid lines represent theoretical calculations by assuming linear Mach number profiles and isentropic flow for the region between the shock and the body, and the dashed-dotted lines represent the results based on linear density profiles. Note that the center of the cylinder is at $x = 0$ which is not shown in the graphs.

mentioned results. To further compare with the approximation of Lobb,[48] we create a constant coefficient for

$$L = \frac{\beta_s^2}{\theta_s^2 \cos\beta_s} \tag{34}$$

under $M_\infty \to \infty$ and $\gamma = 1.4$, hence reach that $L = 0.5956$. This means that if following the density ratio method of Lobb's, the shock standoff distance for supersonic flows around a circular cylinder may be described as

$$\frac{\delta}{D} = 0.5956\frac{\rho_\infty}{\rho_2}. \tag{35}$$

With comparison to (22), the correlation factor of 0.5956 is relatively high. This however seems reasonable since the flow around a circular cylinder is in fact a two-dimensional problem, where the so-called "3d shock relieving effect" is not considered. For a three-dimensional scenario, for example, a supersonic flow around a sphere, the shock wave would be further compressed against the sphere hence a shorter standoff distance would be formed.

Another theoretical method that would be interesting to compare with is the one developed by Hida.[3] Assuming an incompressible but rotational flow behind the detached shock, he derived an approximation for the distance parameter, $B = \delta + R$, by finding solutions for a transcendental equation

$$C(C^2 - 2C + 8)B^4 + 4(C^2 - 2C - 4)B^2 - 4C^3B^2\log B - C^2(2 + C) = 0, \tag{36}$$

where the constant C is

$$C = \frac{3\left(M_\infty^2 - 1\right)^2}{(3M_\infty^2 - 1)\left(1 + \frac{\gamma-1}{2}M_\infty^2\right)}. \tag{37}$$

According to his method, a limiting value, $\delta/D = 0.1241$, is reached as $M_\infty \to \infty$. However, since C is singular at $M_\infty = 1$, it tends to break down as $M_\infty \to 1$. The result for δ/D obtained by this method is also shown in Fig. 7 in dashed lines. Interestingly, his result appears to sit in-between the solutions based on (33) and (35), and these results agree very closely when the Mach number becomes high, say, above 3 to 4. As a further reference of interest, some limiting values with the variation of M_∞ (for $\gamma = 1.4$) are given in Table I in Appendix B.

B. Use of linear Mach number profiles and linear density profiles

The results shown in Fig. 7 suggest a clear difference for approximating δ between the use of linear Mach number profiles, Equation (32), and the use of linear density profiles, Equation (33). Clearly, formula (32) offers a better agreement. To give more insight, we further plot the variation of the flow properties, say, density ratio ρ/ρ_∞ and Mach number M, in a flow field on the central stagnation streamline for the free stream Mach number $M_\infty = 1.35$, 2, and 5, as shown in Fig. 8, where a normal shock condition is observed on this line. It may be understandable then why the linear density profiles have been adopted in previous studies since they offered a better agreement for the computational results for lower Mach numbers of 1.35 and 2. However, the linear Mach number profiles show a better agreement when $M_\infty = 5$. Perhaps because of this better agreement for both ρ/ρ_∞ and M when M_∞ becomes larger, formula (32) is able to provide a better overall agreement for δ than (33). Further detailed results with the use of linear Mach number profiles and linear density profiles are given in Appendix B (e.g., Figs. 11–13), confirming a better agreement for higher M_∞ with the use of linear Mach number profiles.

C. Extension to free-surface granular flows

Cui and Gray[36] studied supercritical free-surface granular flows around a circular cylinder both numerically and experimentally for a Froude number range up to 6. By analogy, the term "supercritical" is equivalent to supersonic in gas flows, Froude number Fr_∞ is similar to Mach number M_∞, while the avalanche thickness is equivalent to density. In their experimental work, they measured the shock standoff distance against the upstream Froude number, which agrees well with the computational result for higher Froude numbers, say, $\mathrm{Fr}_\infty \geq 2.5$. We now analogously apply (32) (theory-1, with a linear Froude number profile) and (33) (theory-2, with a linear avalanche thickness profile) to work out the corresponding shock standoff distance. The comparison in Fig. 9 shows a mixed picture. For lower Froude numbers, the theoretical results based on the modified Newtonian theory are better agreed with the computational and experimental results; but for higher Froude numbers, the theoretical results show a clear discrepancy though theory-2 looks slightly better.

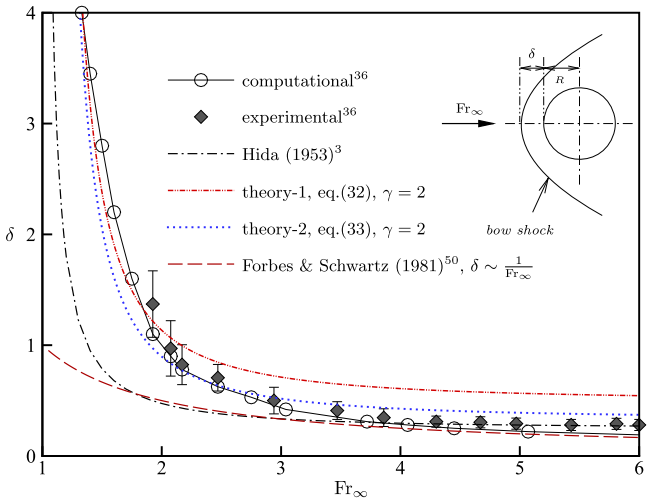

FIG. 9. Shock standoff distance δ against the upstream Froude number Fr_∞ for the granular flow around a circular cylinder. The analogous theoretical results are compared with the results obtained by Cui and Gray.[36] [Reproduced with permission from Cui and Gray, J. Fluid Mech. **720**, 329 (2013). Copyright 2013 Cambridge University Press.]

V. CONCLUSIONS

The modified Newtonian theory, Equation (10), establishes a relation between the pressure coefficient C_p and the angle of the body surface θ. It allows the location of the surface sonic point, parameterized by θ_s and β_s, to be determined if the flow properties in the region bounded between the bow shock wave and the fore part of the body can be known. To achieve this, three conditions have been made. First, the change of the flow properties across the bow shock wave on the stagnation stream line is calculated according to the standard normal shock relations, which is only dependent on the upstream Mach number M_∞. Second, the flow condition after crossing the shock wave is regarded isentropic when no further shock waves occur, which means the total (stagnation) properties, e.g., p_{02} and T_{02}, remain constant in this region. Finally, in order to determine the flow properties, say, p, ρ, T, and M in this region, a further assumption needs to be made, which can be either the "linear density profiles" used in previous studies or the "linear Mach number profiles" adopted in our work.

With the determination of the after-shock flow field and the surface sonic point, the shock standoff distance is approximated by relating it to the variation (or reduction) of the after-shock subsonic region. That is, by letting $b_{ys} = \delta_{M_2}$ (see Sec. III C 3), we have formulated an expression for the shock standoff distance, Equation (32), based on the "linear Mach number profiles" assumption. It has shown an excellent and consistent agreement with the computational solutions and previous experimental results for a broad range of Mach numbers from 1.35 to 6. Other alternative approaches, for example, with the use of the "linear density profiles" or by applying different approximations for b_{ys} and δ_{M_2}, have also been investigated but show no better results. On the other hand, the extension of this method to granular flow problems does not seem to be straightforward. Further extensions to supersonic flows around spheres and to hypersonic flows would be beneficial to provide a broader assessment to the proposed method.

In summary, providing a good theoretical approximation for the shock standoff distance for a wide range of supersonic speeds is obvious and important since the previous theoretical methods have been unable to do so. The proposed method based on the modified Newtonian theory in this paper may offer some useful insights for understanding the basics of supersonic flows. For example, the relation of the surface sonic point hence the after-shock subsonic region with free stream Mach numbers, the surface stagnation and sonic pressures, the isentropic behavior in the after-shock flow field, the use of linear Mach number profiles or linear density profiles, or even the discrepancies between gasdynamic flows and granular flows may help to reveal important physical insights in this field.

ACKNOWLEDGMENTS

The authors wish to acknowledge the support within the community for the valuable suggestions and encouragement.

APPENDIX A: A DESCRIPTION OF THE COMPUTATIONAL METHOD

1. Finite volume approximation

The discretisation of the governing equations using the FVM (finite volume method) is similar to what was used by Jameson *et al.*[51] and Ren.[52] The governing equations are written in the following FVM form, as a control balance equation in two dimensions

$$\frac{\partial}{\partial t}\iint_{\Omega_{i,j}} U dxdy + \oint_{\partial\Omega_{i,j}} H \cdot ndl = 0, \tag{A1}$$

where $\Omega_{i,j}$ is the control volume, $\partial\Omega_{i,j}$ represents its respective boundary, $n = n_x i + n_y j$ is the unit vector normal to the boundary, and U and $H = F_i + G_j$ are the conserved variable and the inviscid flux tensor, respectively.

Using a quadrilateral control volume, the flux through the boundary can be expressed as

$$\frac{\partial}{\partial t}\iint_{\Omega_{i,j}} U dxdy + \sum_{k=1}^{4}\oint_{I_k} H \cdot ndl = 0, \tag{A2}$$

where I_k represents the faces and k denoting each specific face ($k = 1, 2, 3, 4$). Averaging U within the control volume

TABLE I. Limiting values for some important parameters for $M_\infty \to 1$ and $M_\infty \to \infty$, where $\gamma = 1.4$.

M_∞	$M_\infty \to 1$	$M_\infty \to \infty$
M_2[a]	1	0.3780
θ_s (radian)	0	0.8137
ρ_∞/ρ_2	1	1/6
δ/D, based on (32)	∞	0.2251
δ/D, based on (33)	∞	0.0993
δ/D, based on (35)	0.5956	0.0993
δ/D, based on Hida's	Undefined	0.1241

[a]Cross-shock Mach number on the central stagnation stream line.

gives

$$\frac{\partial \overline{U}}{\partial t} = -\frac{1}{|\Omega_{i,j}|}\sum_{k=1}^{4}\int_{I_k} H \cdot ndl = 0. \tag{A3}$$

Integrating the flux terms according to the midpoint rule yields a spatially second order approximation in such a form

$$\frac{\partial \overline{U}}{\partial t} = -\frac{1}{|\Omega_{i,j}|}\sum_{k=1}^{4}(H)_k \cdot (n)_k \Delta I_k, \tag{A4}$$

where ΔI_k denotes the length of I_k. The fluxes are approximated using the Roe Flux Difference Splitting (Roe-FDS) method (see the work of Roe[40]), for example,

$$F_n = \frac{1}{2}(F_{nL} + F_{nR}) - \frac{1}{2}\sum_{k=1}^{4} a_k |\lambda_k| r_k, \tag{A5}$$

where a_k denotes the wave strength, λ_k is an eigenvalue, r_k represents the right eigenvector, and subscripts "L" and "R" represent the left and right fluxes, respectively.

The "least squares cell based" method was selected as the interpolation scheme, which assumes the data between each cell zone vary linearly,

$$\phi_{cf} = \phi_{c0} + (\nabla\phi)_{c0} \cdot \Delta r_f, \tag{A6}$$

where ϕ is the flux variable and r_f represents the vector from the cell centroid $c0$ to the cell face cf. The subscripts f and 0 denote the cell face and center conditions, respectively. Writing similar equations to (A6) in a compact form for each cell surrounding $c0$ gives

$$[J](\nabla\phi)_{c0} = \Delta\phi = (\phi_{cf} - \phi_{c0}), \tag{A7}$$

where $[J]$ is the Jacobian coefficient matrix. The cell gradient $\nabla\phi$ is then calculated from this "over determined" linear system of equations by decomposing the composition matrix using the Gram-Schmidt process, a procedure detailed by Anderson.[53] For this two dimensional cell centered scheme, a matrix of weights for each cell is found, with a separate weight component for each cell face W^x_{i0} and W^y_{i0}. Thus, the gradient at the cell center is found by multiplying the said weights by the difference vector $\Delta\phi$, hence we have

$$(\phi_x)_{c0} = \sum_{i=1}^{N} W^x_{i0}(\phi_{cf} - \phi_{c0}), \tag{A8}$$

$$(\phi_y)_{c0} = \sum_{i=1}^{N} W^y_{i0}(\phi_{cf} - \phi_{c0}). \tag{A9}$$

In the summation N represents the number of edges that connect to the cell. A similar process is shown by Anderson and Bonhaus[54] with further details relating to the calculation of the weights.

2. Boundary conditions

A pressure far field boundary is used for this numerical study with the free stream conditions $P_\infty = 101\,350$ Pa, $T_\infty = 300$ K, and $1.35 \leqslant M_\infty \leqslant 6$. It can only be used alongside the ideal gas law; for the compressible flow this is given as

$$\rho = \frac{p_{op} + p}{\frac{R_g}{M_w}T}, \tag{A10}$$

where p_{op} and p are the operating and local relative pressures, respectively, R_g is the ideal gas constant, M_w is the molecular weight, and T is the static temperature.

The far field is based on Riemann invariants where this non-reflective boundary condition computes the flow variable based on incoming and outgoing waves. Thus, the normal velocity, V_n, on the wall and the local speed of sound, a, are obtained as

$$V_{n_b} = \frac{1}{2}(R^+ + R^-), \tag{A11}$$

$$a_b = \frac{\gamma - 1}{4}(R^+ - R^-), \tag{A12}$$

where γ is the specific heat ratio, R^+ denotes the Riemann invariant for an internal grid (outgoing wave) and R^- for a far field value (incoming wave) detailed by Anderson and Bonhaus[54] and Carlson,[55] and the subscript b denotes the boundary condition. For this computation, the flow is locally supersonic entering and leaving the domain, so the following equations are valid

$$R^+ = V_{n_i} - \frac{2a_i}{\gamma - 1}, \tag{A13}$$

$$R^- = V_{n_o} + \frac{2a_o}{\gamma - 1}, \tag{A14}$$

with the subscripts i and o representing incoming and outgoing characteristics, respectively. Consequently, the tangential velocity V_θ and entropy S are extrapolated from the interior by

$$V_\theta = \frac{xu - yv}{\sqrt{x^2 + y^2}}, \tag{A15}$$

$$S = c_v\left[\frac{p/p_{ref}}{(\rho/\rho_{ref})^\gamma} - 1\right], \tag{A16}$$

where c_v is the specific heat at constant volume and the subscript $_{ref}$ represents free stream conditions. The remaining boundary values such as u_b, v_b, ρ_b, and p_b are then found using

$$u_b = u_{ref} + \hat{n}_x(V_{n_b} - V_{n_{ref}}), \tag{A17}$$

$$v_b = v_{ref} + \hat{n}_y(V_{n_b} - V_{n_{ref}}), \tag{A18}$$

with $\hat{n}$ being the normal unit vector in the x or y direction, and

$$\rho_b = \left(\frac{a_b^2}{\gamma S_b}\right)^{\frac{1}{\gamma-1}}, p_b = \frac{\rho_b a_b^2}{\gamma}, \tag{A19}$$

and the temperature is simply extrapolated from (A10).

Obviously, the inviscid nature of the flow means a slip-wall boundary is enforced at the body surface. These computations are performed on an unstructured quadrilateral grid to allow a better flexibility for adapting the grid as needed.

APPENDIX B: SOME FIGURES AND TABLES

The appendix gives some further figures and tables that may be helpful to gain a more detailed picture for the relevant topics. This includes the following: the limiting values for some important parameters used in the approximation study,

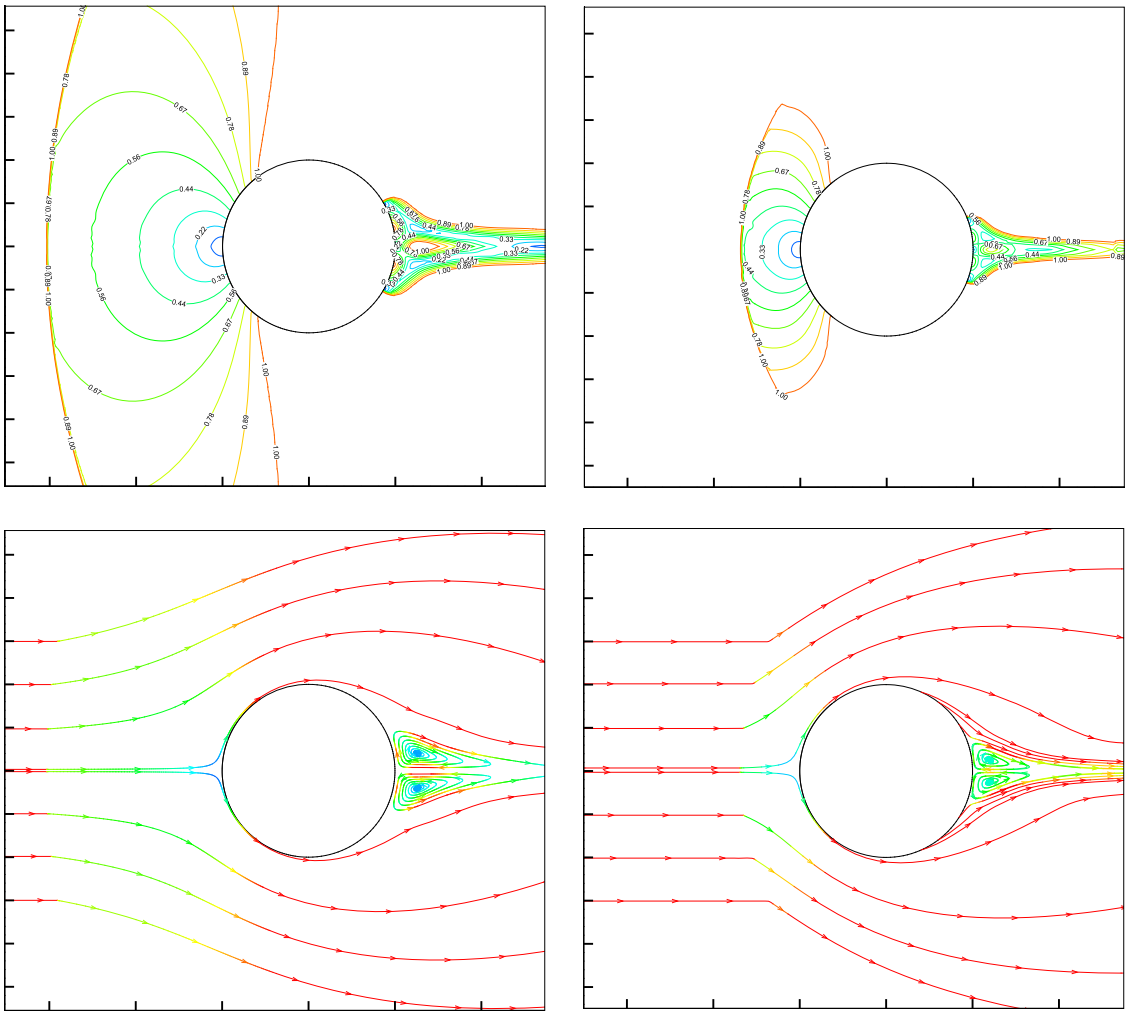

FIG. 10. The after-shock subsonic region for different Mach numbers (top panel), where the left hand side is for $M_\infty = 1.7$ and the right hand side for $M_\infty = 3$. The images at the bottom panel show streamlines around the cylinder, where the recirculation zones at the rear of the cylinder are clearly shown stable (computational results).

as given in Table I; the after-shock subsonic region for different Mach numbers and corresponding streamlines around the cylinder, as shown in Fig. 10; the variation of the total temperature and total pressure around the shock waves, as shown in Fig. 11; the variation of the flow properties across the shock waves, as shown in Figs. 12 and 13.

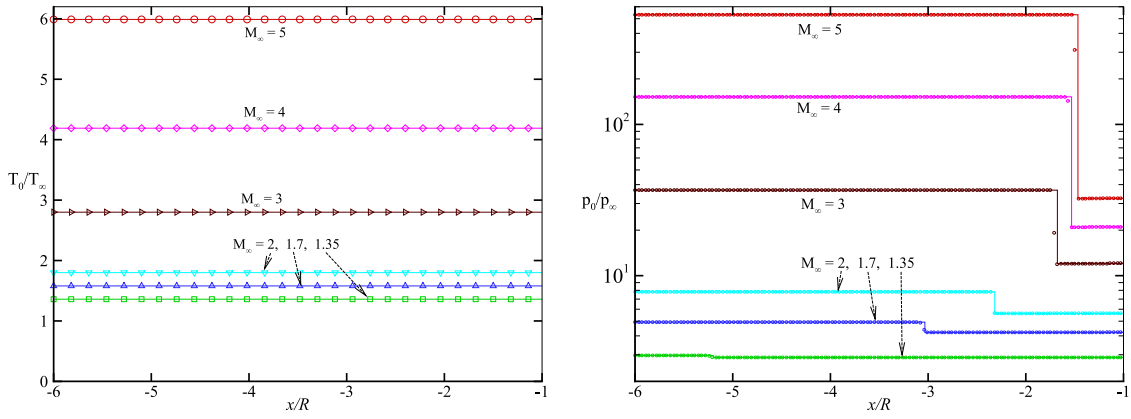

FIG. 11. Variation of T_0/T_∞ and p_0/p_∞ with x/R on the central stagnation stream line for $M_\infty = 1.35, 1.7, 2, 3, 4, 5$. The scattered symbols denote computational results and the solid lines represent theoretical calculations. Note that for the pressure ratio on the right hand side, the vertical axis is given in the logarithm scale. From these two graphs, it shows clearly the conservation of the stagnation temperature across the shocks, and the stagnation pressure drops across the shocks but is then conserved before reaching the surface of the cylinder ($x/R = -1$). Therefore, the flow field between the shock and the front of the cylinder behaves isentropically.

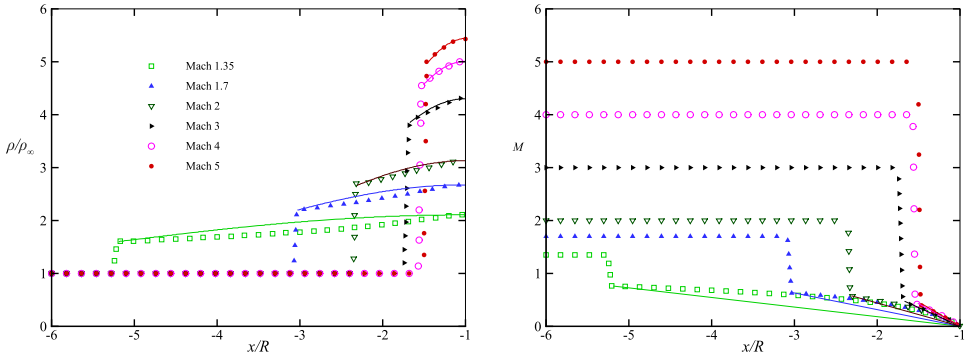

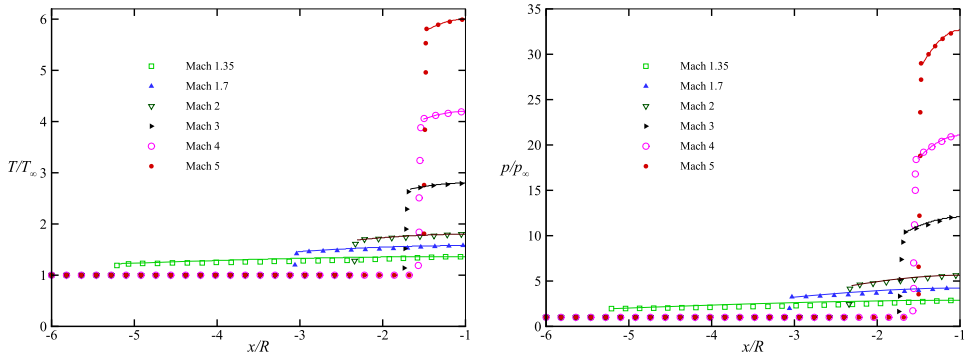

FIG. 12. Variation of ρ/ρ_∞, M, T/T_∞, and p/p_∞ with x/R on the central stagnation stream line for $M_\infty = 1.35, 1.7, 2, 3, 4, 5$. The scattered symbols represent computational results and the solid lines represent theoretical calculations by assuming *linear Mach number profiles* and isentropic flow for the region between the shock and the body. Note that the center of the cylinder is at $x/R = 0$ which is not shown in the graphs.

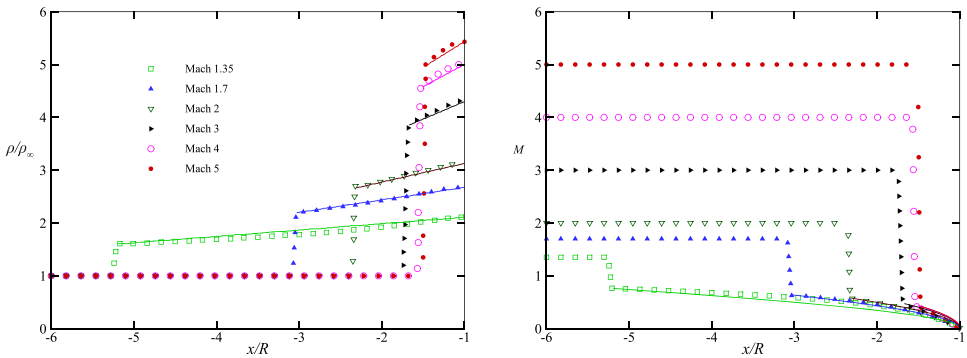

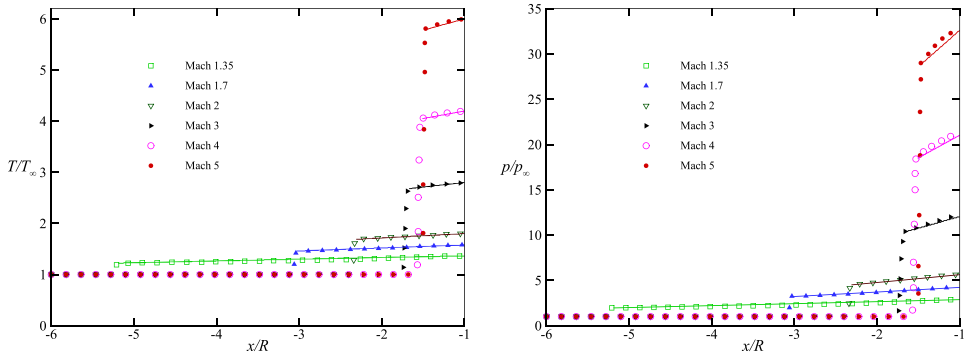

FIG. 13. Variation of ρ/ρ_∞, M, T/T_∞, and p/p_∞ with x/R on the central stagnation stream line for $M_\infty = 1.35, 1.7, 2, 3, 4, 5$. The scattered symbols represent computational results and the solid lines represent theoretical calculations by assuming *linear density profiles* and isentropic flow for the region between the shock and the body.

[1]G. Moretti, "Computation of flows with shocks," Annu. Rev. Fluid Mech. **19**, 313–337 (1987).
[2]W. E. Moeckel, "Approximate method for predicting the form and location of detached shock waves ahead of plane or axially symmetrical bodies," NACA Technical Note 1921, 1949.
[3]K. Hida, "An approximate study of the detached shock wave in front of a circular cylinder and a sphere," J. Phys. Soc. Japan **8**, 740–745 (1953).
[4]M. J. Lighthill, "Dynamics of a dissociating gas. Part I: Equilibrium flow," J. Fluid Mech. **2**, 1–32 (1957).
[5]M. Alperin, "A study of detached shock waves in two-dimensions," Ph.D. thesis, CIT, 1950.
[6]M. D. Van Dyke, "The supersonic blunt-body problem—Review and extension," J. Aerosp. Sci. **25**, 485–496 (1958).
[7]C.-S. Kim, "Experimental studies of supersonic flow past a circular cylinder," J. Phys. Soc. Japan **11**(4), 439–445 (1956).
[8]W. E. Moeckel, "Experimental investigation of supersonic flow with detached shock waves for Mach numbers between 1.8 and 2.9," NACA RM E50D05, 1950.
[9]J. W. Heberle, G. P. Wood, and P. B. Gooderum, "Data on shape and location of detached shock wave on cones and spheres," NACA Technical Note 2000, 1950.
[10]A. F. Bryson, "An experimental investigation of transonic flow past two-dimensional wedge and circular arc section using a Mach-Zehnder interferometer," Ph.D. thesis, CIT, CA, 1951.
[11]K. Hida, "Blunt body theory for hypersonic flow," Air Force Office of Scientific Research, Guggenhiem Aeronautical Laboratory, CIT, 1961.

[12]G. E. Kaattari, "Predicting shock envelopes about two types of vehicles at large angles of attack," NASA Technical Note D-860, 1961.
[13]W. K. Osborne and F. W. Crane, "Flow field and pressure distribution measurements on blunt-nosed bodies at $M = 6.8$," GB Aeronautical Research Council C.P. No. 615, 1962.
[14]G. E. Kaattari, "A method for predicting shock shapes and pressure distributions for a wide variety of blunt bodies at zero angle of attack," NASA Technical Note D-4539, 1968.
[15]K. S. Nagaraia, "On the shock stand-off distance in an inviscid hypersonic source flow past two-dimensional bluff bodies," ARL 71-0303, 1971.
[16]O. M. Beletoserkovski, *Flow Past a Circular Cylinder with a Detached Shock* (Academy of Sciences, Moscow, 1958).
[17]F. M. Hamaker, "Numerical solution of the flow of a perfect gas around a circular cylinder at infinite Mach number," NASA MEMO 2-25-59A, 1959.
[18]D. C. Thoman and A. A. Szewczyk, "Time-dependent viscous flow over a circular cylinder," Phys. Fluids **12**, II-76 (1969).
[19]J.-Y. Yang, Y. Liu, and H. Lomax, "A numerical study of shock wave diffraction by a circular cylinder," in *AIAA, Aerospace Sciences Meeting* (AIAA, 1986), p. 12.
[20]H. G. Hornung, "Non-equilibrium dissociating nitrogen flow over spheres and circular cylinders," J. Fluid Mech. **53**, 149–176 (1972).
[21]C.-Y. Wen and H. G. Hornung, "Non-equilibrium dissociating flow over spheres," J. Fluid Mech. **299**, 389–405 (1995).
[22]R. C. M. Trivandrum, "Numerical investigation of viscous flow over a hemisphere-cylinder," Acta Mech. **128**(1-2), 49–58 (1998).
[23]T. Mizukaki, "Detached shock waves around cylinders flying at Mach number ranging from 1 to 2," J. Visualization **11**(2), 133–141 (2008).
[24]M. Sharma, A. B. Swantek, W. Flaherty, J. M. Austin, S. Doraiswamy, and G. V. Candler, "Experimental and numerical investigations of hypervelocity carbon dioxide flow over blunt bodies," J. Thermophys. Heat Transfer **24**, 673–683 (2010).
[25]F. Zander, R. J. Gollan, P. A. Jacobs, and R. G. Morgan, "Hypervelocity shock standoff on spheres in air," Shock Waves **24**, 171–178 (2014).
[26]T. Nagata, T. Nonomura, S. Takahashi, Y. Mizuno, and K. Fukuda, "Investigation on subsonic to supersonic flow around a sphere at low Reynolds number of between 50 and 300 by direct numerical simulation," Phys. Fluids **28**, 056101 (2016).
[27]J. M. N. T. Gray, Y.-C. Tai, and S. Noelle, "Shock waves, dead-zones and particle-free regions in rapid granular free surface flows," J. Fluid Mech. **491**, 161–181 (2003).
[28]J. M. N. T. Gray and X. Cui, "Weak, strong and detached oblique shocks in gravity-driven granular free-surface flows," J. Fluid Mech. **579**, 113–136 (2007).
[29]J. F. Boudet, Y. Amarouchene, and H. Kellay, "Shock front width and structure in supersonic granular flows," Phys. Rev. Lett. **101**, 254503 (2008).
[30]S. H. Chou, L. S. Lu, and S. S. Hsiau, "DEM simulation of oblique shocks in gravity-driven granular flows with wedge obstacles," Granular Matter **14**, 719–732 (2012).
[31]K. M. Hákonardóttir and A. J. Hogg, "Oblique shocks in rapid granular flows," Phys. Fluids **17**, 0077101 (2005).
[32]P. Heil, E. C. Rericha, D. I. Goldman, and H. L. Swinney, "Mach cone in a shallow granular fluid," Phys. Rev. E **70**, 060301 (2004).
[33]D. A. Padgett, A. P. Mazzoleni, and S. D. Faw, "Survey of shock-wave structures of smooth-particle granular flows," Phys. Rev. E **92**, 062209 (2015).
[34]S. P. Pudasaini and C. Kröner, "Shock waves in rapid flows of dense granular materials: Theoretical predictions and experimental results," Phys. Rev. E **78**, 041308 (2008).
[35]X. Cui, "Computational and experimental studies of rapid free-surface granular flows around obstacles," Comput. Fluids **89**, 179–190 (2014).
[36]X. Cui and J. M. N. T. Gray, "Gravity-driven granular free-surface flow around a circular cylinder," J. Fluid Mech. **720**, 314–337 (2013).
[37]M. Abbett and G. Moretti, "A time-dependent computational method for blunt body flows," AIAA J. **4**(12), 2136–2141 (1966).
[38]A. Harten, "High resolution schemes for hyperbolic conservation laws," J. Comput. Phys. **49**, 357–393 (1983).
[39]H. Nessyahu and E. Tadmor, "Non-oscillatory central differencing for hyperbolic conservation laws," J. Comput. Phys. **87**, 408–463 (1990).
[40]P. L. Roe, "Approximate Riemann solvers, parameter vectors, and difference schemes," J. Comput. Phys. **43**(2), 357–372 (1981).
[41]S. K. Godunov, "A difference method for numerical calculation of discontinuous solutions of the equations of hydrodynamics," Mat. Sb **47**, 271–306 (1959).
[42]J. F. Daunenhofer and J. R. Baron, "Grid adaption for the 2D Euler equations," AIAA Paper No. 85-0484, 1985.
[43]M. D. Salas, "Recent developments in transonic Euler flow over a circular cylinder," NASA TM 83282, 1982.
[44]M. Pandolfi and F. Larocca, "Transonic flow about a circular cylinder," Comput. Fluids **17**, 205–220 (1989).
[45]N. Botta, "The inviscid transonic flow about a cylinder," J. Fluid Mech. **301**, 225–250 (1995).
[46]M. Hafez and E. Wahba, "Inviscid flows over a cylinder," Comput. Methods Appl. Mech. Eng. **193**, 1981–1995 (2004).
[47]L. Lees, "On the boundary layer equations in hypersonic flow and their approximate solutions," in Proceedings of the 5th International Aeronautical Conference (IAS-RAS), Hypersonic Flow [J. Aero. Sci. **20**, 143–145 (1953)].
[48]R. K. Lobb, "Experimental measurement of shock detachment distance on spheres fired in air at hypervelocities," Defense Technical Information Center, 1962.
[49]H. Olivier, "A theoretical model for the shock stand-off distance in frozen and equilibrium flows," J. Fluid Mech. **413**, 345–353 (2000).
[50]L. K. Forbes and L. W. Schwartz, "Supercritical flow past blunt bodies in shallow water," Z. Angew. Math. Phys. **32**, 314–328 (1981).
[51]A. Jameson, W. Schmidt, and E. Turkel, "Numerical solution of the Euler equations by finite volume methods using Runge-Kutta time-stepping schemes," AIAA Paper No. 81-1259, 1981.
[52]Y.-X. Ren, "A robust shock-capturing scheme based on rotated Riemann solvers," Comput. Fluids **32**, 1379–1403 (2003).
[53]W. K. Anderson, "Grid generation and flow solution method for Euler equations on unstructured grids," NASA/TM 4295, 1992.
[54]W. K. Anderson and D. L. Bonhaus, "An implicit upwind algorithm for computing turbulent flows on unstructured grids," Comput. Fluids **23**(1), 1–21 (1994).
[55]J. R. Carlson, "Inflow/outflow boundary conditions with application to FUN3D," NASA/TM-2011–217181, 2011.